



Magmatic subsidence of the East Pacific Rise (EPR) at 18°14'S revealed through fault restoration of ridge crest bathymetry

Suzanne M. Carbotte, William B. F. Ryan, Wen Jin, and Marie-Helene Cormier

Lamont-Doherty Earth Observatory, 61 Rte 9W, Palisades, New York 10964, USA (carbotte@ldeo.columbia.edu)

Eric Bergmanis and John Sinton

Department of Geology and Geophysics, University of Hawaii, 2525 Correa Road Honolulu, Hawaii 96822, USA

Scott White

Geological Sciences Department, University of South Carolina, Columbia, South Carolina 29209, USA

[1] The fault restoration technique of *De Chabaliere and Avouac* [1994] is applied to an ultra-high-resolution bathymetry data set from the East Pacific Rise (EPR) at 18°14'S. Fault offsets are calculated and subtracted from the original seafloor bathymetry to examine the morphology of the unfaulted seafloor surface within an area encompassing the ridge axis 400 × 1600 m in dimension. The restored topography reveals a gently sloping seafloor ~200 m wide, which slopes 5° inward toward the spreading axis. We attribute this inward sloping seafloor to subsidence within the axial trough due to subsurface magmatic deflation. The vertical deformation field extracted from the bathymetry is used to characterize the ridge axis fault population present in the area. Median fault throws (9 m for inward-facing and 8 m for outward-facing faults) are comparable to values measured for nearby mature abyssal hill fault populations, suggesting a genetic link. However, median fault spacings (70 and 46 m) are an order of magnitude smaller, and estimated total extensional strain is 3×–4× greater than values measured for ridge flank faults. These differences indicate the axial fault population at 18°14'S cannot be rafted onto the ridge flanks to form abyssal hill faults without significant modification, presumably via volcanic burial. We attribute the dense faulting observed in this area to slip on axial fissures during subsidence of the crestal region. The surface subsidence of a volcanic edifice can be modeled in terms of volume change in the magma source reservoir and volume of magma withdrawn from the reservoir. Using the relationship derived for a sill-like magma body, we estimate that the axial depression at 18°14'S could represent magma withdrawal associated with a small number (4–22) of the frequent dike injection and eruption events required to build the upper crust during the evolution of the trough. The subsidence volumes represented by the axial topography at 18°14'S are a small percentage of the underlying upper crustal sections (3–4%), suggesting that only a minor mismatch between magma recharge and withdrawal from the axial melt lens during ongoing plate separation could account for this pronounced axial depression.

Components: 10,874 words, 9 figures, 3 tables.

Keywords: Midocean ridge; East Pacific Rise; axial trough; faults; magmatic subsidence; autonomous underwater vehicle.

Index Terms: 3035 Marine Geology and Geophysics: Midocean ridge processes; 3045 Marine Geology and Geophysics: Seafloor morphology and bottom photography; 8145 Tectonophysics: Physics of magma and magma bodies.

Received 2 March 2002; **Revised** 10 September 2002; **Accepted** 12 September 2002; **Published** 23 January 2003.

Carbotte, S. M., W. B. F. Ryan, W. Jin, M.-H. Cormier, E. Bergmanis, J. Sinton, and S. White, Magmatic subsidence of the East Pacific Rise (EPR) at 18°14'S revealed through fault restoration of ridge crest bathymetry, *Geochem. Geophys. Geosyst.*, 4(1), 1008, doi:10.1029/2002GC000337, 2003.

1. Introduction

[2] In 1994, De Chabali er and Avouac published an innovative study of deformation of the Fieale Volcano within the Asal Rift, a subaerial counterpart of a slow spreading mid-ocean ridge where ongoing stretching and volcanism can be observed directly. From a high-resolution digital elevation model (DEM) of the region, De Chabali er and Avouac determined the deformation field of the active rift and through restoration of fault offsets, were able to quantify the relative contribution of volcanic and tectonic processes to rifting. Comparisons of the amount of topographic subsidence with the horizontal extension revealed that magmatic intrusion must accommodate nearly all the crustal stretching in this region. With the restored topography, the authors also showed that fault blocks at this slow-spreading rift were not back tilted as had previously been assumed and that the disruption of the Fieale Volcano was likely due to caldera collapse in an extensional environment. The quantitative approach demonstrated in this study was possible because spreading occurs in an accessible terrestrial setting and a very high resolution DEM was available for the region from space-imaged and field-mapped topography.

[3] In spring 1999, ultra-high-resolution Imagenex bathymetric data were acquired for two sites along the Southern East Pacific Rise (EPR) using the Autonomous Benthic Explorer (ABE) vehicle [Cormier *et al.*, 1999; Yoerger *et al.*, 2000a, 2000b; Shah *et al.*, 2002]. These data were collected as part of a near bottom mapping and sampling investigation of ridge crest volcanology between 17° and 19°S (the STOWA expedition, [Sinton *et al.*, 2002]). The vertical resolution of the bathymetry data (<30 cm) is unprecedented for seafloor settings and exceeds that of most DEM data sets

available on land, including that used in the study of the Fieale volcano. In this contribution we use data collected from the 18°14'S site to demonstrate the method of De Chabali er and Avouac for analysis of volcanic and tectonic processes at mid-ocean ridges. Our study involves two components; 1) calculation of the vertical displacement field and characterization of fault parameters for the ridge crest fault population present at 18°14'S, and 2) removal of this displacement field to reconstruct the unfaulted seafloor surface. Long-wavelength (100s of meters) changes in seafloor slope are revealed in the resulting "restored" seafloor surface, which are interpreted in terms lava flow emplacement processes, and postemplacement deformation associated with tectonic and magmatic processes. Side-scan sonar data and near bottom visual observations provide ground truth data for our interpretations. The restored seafloor surface and characteristics of the axial fault population provide evidence for subsidence of the crestal region in response to subsurface magmatic deflation. Elastic models for magma chamber inflation/deflation and relations derived from terrestrial studies are used to compare the subsidence volumes represented by the axial topography at 18°14'S to the predicted volume change within the midcrustal magma lens and to eruptive and intrusive volumes. We conclude that the development of the axial depression at 18°14'S could reflect magma withdrawal associated with only a small subset of the frequent dike injection/volcanic eruption events which build the upper crust in a system where magma resupply and withdrawal do not always keep pace.

2. Geological Setting

[4] The study area lies within a 20 km long segment of the EPR [segment Js, Sinton *et al.*, 1991]

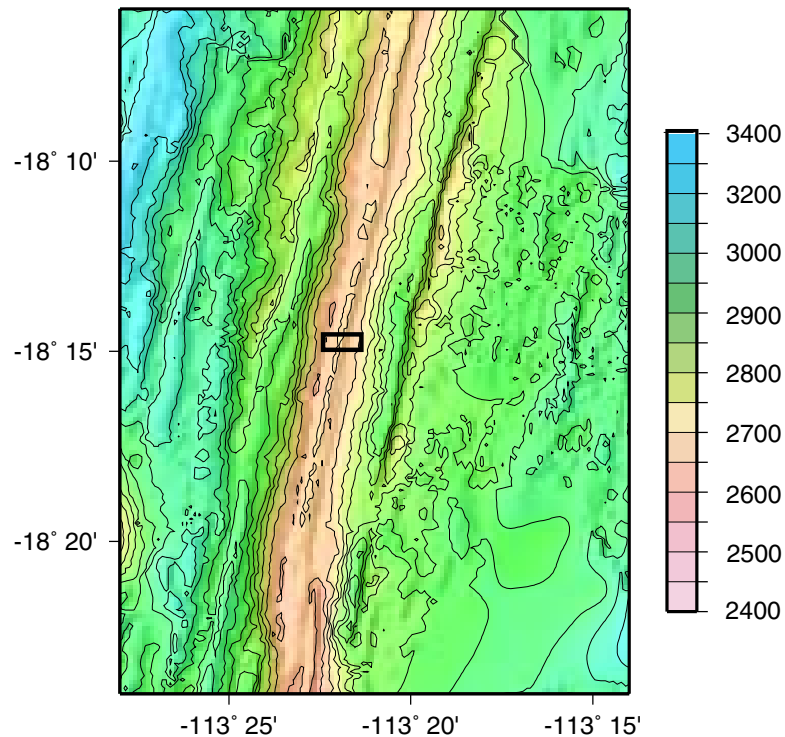


Figure 1. (a) Multibeam bathymetric map of the southern EPR [from *Cormier et al.*, 1997] showing location of study area (black rectangle). Contour interval is 50 meters. (b) Ultra-high-resolution bathymetric data for the study area. Data were collected with the Imagenex pencil scanning sonar with a vertical resolution >30 cm and a horizontal resolution of 5 m along track and 2 m cross-track [Yoerger *et al.*, 2000a, 2000b]. Track lines were spaced every 30 m and navigation was accomplished using acoustic ranging within a transponder net. Data are gridded using the Delauney triangulation gridding algorithm of GMT [Wessel and Smith, 2001]. Contours are drawn every 2 meters with interpolated areas masked. Map coordinates are shown in both latitude-longitude (north and west axis) and the x - y coordinate framework of the transponder net (in meters, south and east axis). Major morphological features are labeled. Track of Alvin dive 3355 through the study area is shown in red. Rock samples recovered during dive are numbered and color coded for MgO values from Table 1; red >8.0 , and green >7.0 . A–A' delimits segment of Alvin profile shown in Figure 3. Stars show location of persistent left stepping offset at $18^{\circ}14'47''$ S.

bounded by small ridge offsets located at $18^{\circ}22'S$ and $18^{\circ}10'S$ (Figure 1a). A prominent axial trough, ~ 50 m deep and 250–600 m wide, extends the full length of this segment. This region contrasts markedly with the ridge axis north of $17^{\circ}55'S$ where a smooth domal crest is found with occasional lava flow collapse features and fissures [Auzende *et al.*, 1996; Lagabrielle and Cormier, 1999; White *et al.*, 2000]. Imagenex bathymetry collected during the STOWA cruise included a site at $17^{\circ}28'S$ where an effusive lobate lava flow, believed to have erupted in the early 1990s, was mapped [Cormier *et al.*, 1999; Shah *et al.*, 2002]. Lagabrielle and Cormier [1999] suggest that the prominent axial trough south of $17^{\circ}55'S$ may have

developed only recently and that the axis formerly displayed a domal morphology similar to that present to the north.

3. Geological Observations

3.1. Bathymetric Data

[5] The Imagenex bathymetry data cover an area $\sim 400 \times 1600$ m centered on the crest of the axial high. In this area, the locus of active accretion lies within an asymmetric trough which is ~ 600 m wide and up to 60 m deep. The western shoulder of the trough is a smooth terrain disrupted by a prominent graben 150 m wide and 15 m deep.

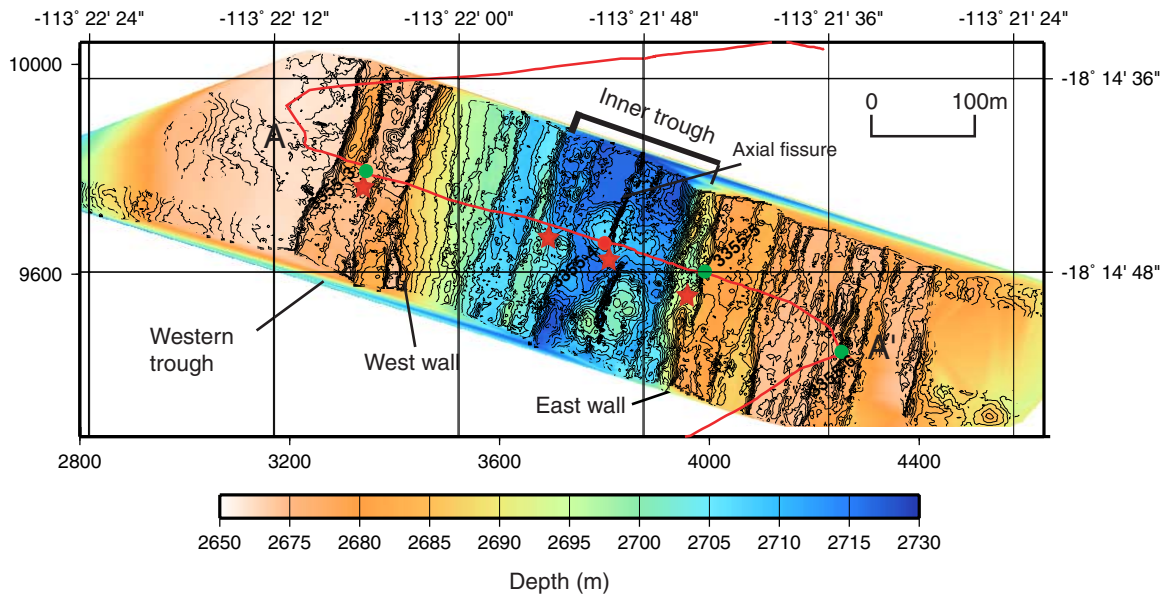


Figure 1. (continued)

This feature has been interpreted as a volcanic collapse structure, formed by drainback and drain out of lava associated with an effusive lobate eruption, analogous to the $17^{\circ}28'$ flow [White *et al.*, 2000; Shah *et al.*, 2002]. However, the walls of this depression are not scalloped in plan view as expected for a collapsed volcanic roof remnant but rather are linear scarps that extend for several kilometers. If this depression were a volcanic collapse feature, the linear walls indicate significant subsequent tectonism. In this paper, we refer to this graben as the western trough (Figure 1b). East of the western trough seafloor steps down along a series of predominantly inward, axis-facing scarps to reach depths of 2730 m. The deepest part of the axial trough corresponds with a 200-m-wide graben (inner trough, Figure 1b). Two roughly circular, domal mounds rise from this innermost trough floor. The southern volcanic mound is larger in plan view and almost twice the height of the northern mound (35–40 m compared with 20–24 m). An en echelon fissure (referred to as the axial fissure), which is 10–15 m wide and 10 m deep, dissects both mounds. This fissure steps left by 35 m at $18^{\circ}14'47''S$, $113^{\circ}21'50''W$. The eastern wall of the axial trough is a prominent, multi-stepped inward-facing scarp up to 60 m high (east wall, Figure 1). In contrast to the smooth western shoulder, the eastern shoulder of the trough is

heavily disrupted by a series of both inward- and outward-facing faults.

[6] Several fault scarps within the axial trough display left-stepping offsets at the same location as the volcanic mounds of the trough floor (Figure 1b). The faults bounding the inner trough floor step left by 65 meters at $\sim 18^{\circ}14'47''S$. The western trough is segmented at the same location along the ridge with a left stepping jog of 95 m evident in the deepest part of this depression. Also at this same location, the western wall of the axial trough diminishes in throw and changes strike.

3.2. Side-Scan Sonar Data

[7] High resolution DSL 120 kHz side-scan sonar imagery are available for most of the axial region of the $18^{\circ}10'–22'S$ segment, including the area surveyed with Imagenex bathymetry (Figure 2). These data provide useful constraints on relative lava ages as well as the location of fine-scale seafloor fractures and local volcanic constructs beyond the Imagenex bathymetric coverage [e.g., Scheirer *et al.*, 2000]. The side-scan data reveal low backscatter amplitudes from the western shoulder. Backscatter amplitudes within the western trough are indistinguishable from those of the surrounding shoulder terrain indicating that lavas,

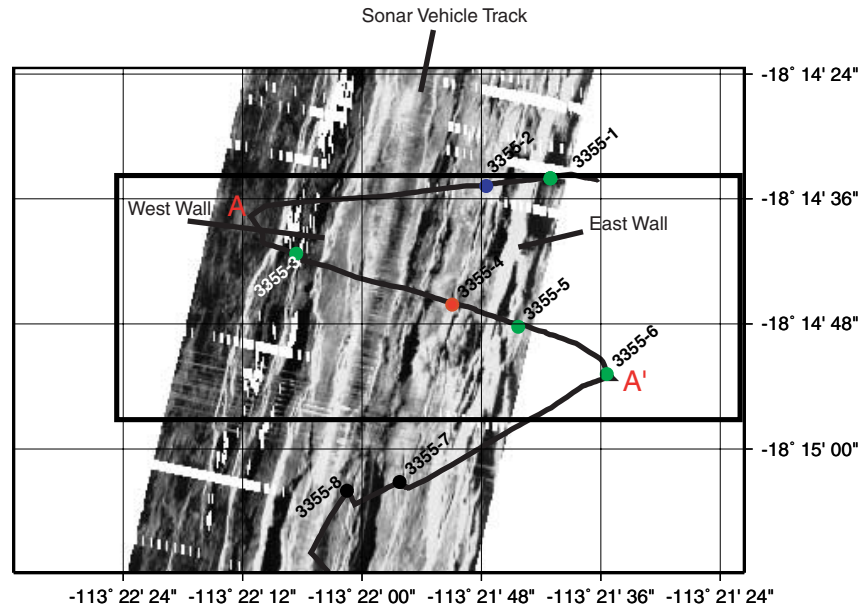


Figure 2. DSL 120 kHz side scan sonar data for the study area collected with ARGO II in 1996 during the Sojourn 2 cruise [Haymon *et al.*, 1997; White *et al.*, 2000]. Low backscatter values are in black and high backscatter in white. Walls of the axial trough are labeled. Black box shows the area of Figure 1. Track of Alvin dive 3355 through the study area is shown in black with segment A–A' of Figure 3 indicated. Rock samples recovered during dive are color coded for MgO values from Table 1; red >8.0, green >7.0, blue >6.0.

which floor this depression, are close in age. A stepwise increase in backscatter amplitude occurs across the west wall of the axial trough, indicating that lavas within the axial trough are younger than the west shoulder terrain (Figure 2). Within the floor of the axial trough, the highest backscatter values are associated with the domal volcanic

mounds, which could reflect higher bathymetric gradients or lower sediment cover.

3.3. Alvin Observations

[8] One Alvin dive was carried out through the study area, providing direct observations of lava

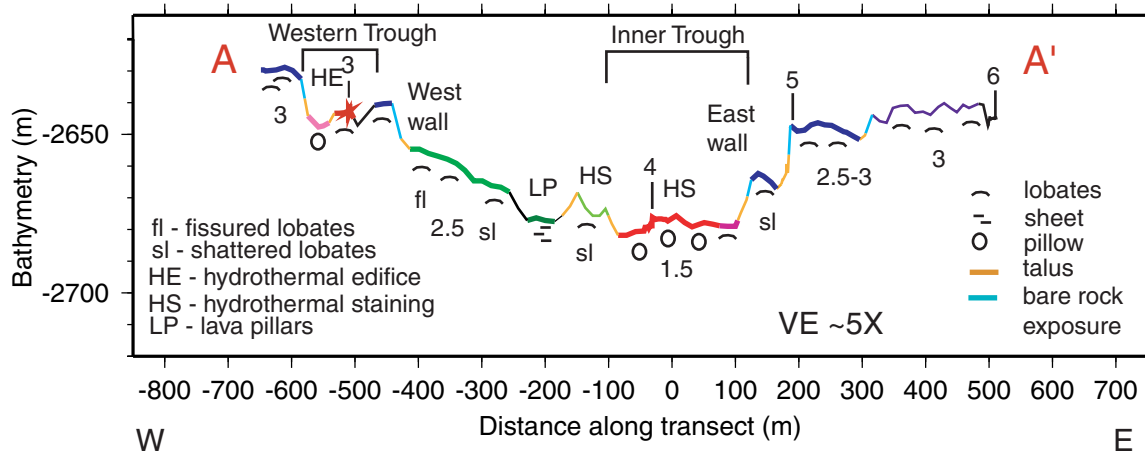


Figure 3. Alvin bathymetry and summary of visual observations along segment A–A' of dive 3355 (see Figures 1 and 2 for location). Flow morphology is indicated by symbols below the profile and numbers correspond to lava ages interpreted from visual estimates of sediment cover. Colored segments along the bathymetric profile show lavas interpreted to be related flow units. Numbered sites above profile correspond with rock sample locations also shown in Figures 1 and 2.

Table 1. Major-Element Analyses of Natural Glasses From Alvin Dive 3355

	3355-1	3355-2	3355-3	3355-4	3355-5	3355-6	3355-7	3355-8
SiO ₂	50.6	50.0	50.5	49.7	50.6	50.6	50.3	50.4
TiO ₂	1.54	2.27	1.53	1.32	1.57	1.51	1.53	1.63
Al ₂ O ₃	14.7	13.8	14.7	15.9	14.6	14.7	14.9	14.6
FeO ^a	10.3	12.6	10.4	9.5	10.6	10.4	10.2	10.6
MnO	0.21	0.23	0.19	0.19	0.20	0.22	0.19	0.20
MgO	7.68	6.49	7.68	8.36	7.36	7.64	7.77	7.60
CaO	12.1	10.9	12.1	12.4	11.9	12.2	12.3	11.8
Na ₂ O	2.74	2.99	2.78	2.60	2.89	2.79	2.63	2.82
K ₂ O	0.06	0.13	0.06	0.05	0.07	0.06	0.10	0.07
P ₂ O ₅	0.11	0.20	0.11	0.11	0.12	0.10	0.12	0.11
Total	100.1	99.6	100.1	100.1	99.9	100.1	100.0	99.8
Lat (S)	18°14.64′	18°14.58′	18°14.70′	18°14.76′	18°14.82′	18°14.88′	18°15.06′	18°15.06′
Long (W)	113°21.60′	113°21.78′	113°22.14′	113°21.84′	113°21.72′	113°21.60′	113°21.96′	113°22.02′
Depth	2645	2689	2641	2677	2647	2643	2689	2664

All analyses by University of Hawaii electron microprobe.

^aTotal iron reported as FeO.

morphology, fissures, fault scarps, talus presence and extent of sediment cover (Figure 3). On the western shoulder, the dive transect reveals a heavily sedimented terrain of smooth unfractured lobate flows which are completely buried in places with sediment thicknesses of ~2.5 to 10 cm. Lavas on the rims of the western trough are indistinguishable from the lobate lavas of the unfractured western shoulder and are interpreted to be the same flows. Within the floor of the western trough an extinct hydrothermal edifice and sedimented pillow lavas are observed, which appear to postdate the collapsed lobate flows.

[9] Using reported sedimentation rates for the area of 0.3–2.6 cm/1000 yr [Marchig *et al.*, 1986; Dekov and Kuptsov, 1992], estimated sediment thicknesses provide a wide possible age range of 1000 to 33,000 years for the west shoulder lavas. However, accumulation of hydrothermal sediments and local sediment redistribution via bottom currents [e.g., Marchig *et al.*, 1986] may bias these estimates to older ages. Additional constraints on lava ages are provided by the spreading age of the seafloor which, for lobate flows, represent a likely maximum age as these flows can extend for up to several kilometers from their eruption sources [e.g., Sinton *et al.*, 2002]. In the absence of dated samples, we assume the spreading age for the eastern edge of the western shoulder (4000 years) represents the likely maximum age for the west

shoulder lavas and we use 3000–4000 years as our best guess age range for these lavas.

[10] East of the west wall, fissured lobate flows grading into highly shattered lobate flows form a gently east-sloping seafloor (Figure 3). These flows are less sedimented than the lavas of the trough shoulder, consistent with the younger age inferred from the side-scan sonar data. Further to the east, a 65–95 m wide graben is observed, which is floored by sheet flows with abundant evidence for volcanic collapse structures including lava pillars with uncollapsed roof remnants [e.g., Gregg and Chadwick, 1996; Fornari *et al.*, 1998]. Beyond this collapsed terrain seafloor steps down into the deepest and least sedimented portion of the axial trough. The domal mounds imaged in the ABE bathymetry are comprised of pillow lavas, with hydrothermal staining and sparse vent animals indicating recent or near-by venting. These pillow mounds are the youngest lavas in the area and overlie older lobate flows, which floor the inner trough. These relative age and stratigraphic relationships indicate that the inner trough represents the modern neovolcanic zone.

[11] Along the dive track, the eastern wall of the axial trough is a stepped fault scarp with bare-rock exposures near the fault crest. At the rim of the trough, heavily sedimented unshattered lobates are observed which appear similar in age to those covering the western shoulder. An increase in sediment cover is evident at the first prominent

fault on this shoulder and lavas east of this fault appear older (Figure 3).

[12] Talus accumulations observed at the base of fault scarps within the main trough show varying degrees of sediment cover, indicating an age progression in tectonic deformation within the trough. Talus piles at the base of the inner trough walls are sediment free indicating recent activity, whereas sediment is visible on talus blocks associated with the west wall indicating no recent activity on this fault.

[13] Rock samples were collected during this dive from the axial shoulders and from various locations within the axial trough including the axial pillow mounds (Figures 1–3; Table 1). Trough shoulder samples 1, 3 and 6, are chemically identical within analytical precision. Although sample 5 is slightly different in most elements, these differences are generally small and are consistent with fractionation in a crustal magma chamber. Other samples display a range of compositions, indicating variable parental magma compositions and extents of magma evolution in this region, over the period of time represented by the sample collections, assumed to be on the order of thousands of years based on spreading age and sediment cover. Pillow mound sample 4 is notably less differentiated (higher MgO) than other samples from the area. *Sinton et al.* [2002] interpreted similar compositions from relatively young pillow mounds and lava shields in the 18°10′–18°22′S region to possibly reflect recent recharge of primitive magmas to this segment.

4. Fault Restoration Methodology

[14] From the gridded bathymetric data (3×2 m grid spacing), we extract a series of profiles oriented perpendicular to the axial trend. Profiles are spaced 3 meters apart and are centered on the axial fissure (Figures 1b, 4–6). Along each profile the location and vertical offset of all faults are determined using a fault detection algorithm which identifies faults where the local topographic gradient exceeds a specified slope threshold (Figure 4) [e.g., *Wilcock et al.*, 1993; *Alexander and Macdonald*, 1996]. Topographic slope resolution from bathymetric data is limited by characteristics of the acquisition sonar

system including acoustic beam width, frequency and ping spacing. With a gridded data set, practical limits on the slopes that can be accurately measured are further constrained by the grid interval (often larger than acoustic footprint or ping spacing) and the vertical relief of a feature, such that steeper slopes can be resolved if the vertical relief is large [e.g., *Kleinrock et al.*, 1992; *Goff and Kleinrock*, 1991]. As a result of these limitations, the threshold slope required to detect all faults within a bathymetric data set is primarily determined by the smallest faults imaged and is much lower than the maximum slope resolution for the data. However, at low slopes, it becomes increasingly difficult to distinguish tectonic relief from volcanic topography, and care must be taken when choosing a slope threshold to avoid flagging volcanic relief.

[15] For our data, we find a threshold angle of 25° is adequate for detecting most inward facing faults and for the outward facing faults within the western portion of the axial trough (Figure 5). A lower threshold angle of 20° is required to identify outward facing faults on the eastern shoulder of the trough, presumably due to the lower average relief of these faults. Visual comparison of the bathymetric data with the slopes flagged using these threshold angles shows that some fine-scale volcanic roughness is detected and the lowest relief portions of faults (e.g., at fault ends) are not always fully identified. These limitations give rise to short-wavelength noise in the restored surface as discussed below. However, fault detection is excellent for scarps >3 m in relief, and fine-scale features of fault scarps such as subtle ramps and splays are remarkably well resolved (Figure 5).

[16] To remove vertical fault displacements from the topography data, the western end of each profile is held fixed at its original elevation and seafloor is shifted up or down at each identified fault by an amount equal to the vertical fault offset (H , Figure 4a). To take into account talus deposition at the base of fault scarps and erosion at fault crests we include with a flagged fault all relief at the top or bottom of fault scarps where the local bathymetric slope is greater than half the input slope threshold (Figure 4). Vertical relief at a fault may differ significantly from the vertical fault throw if the surface slopes of

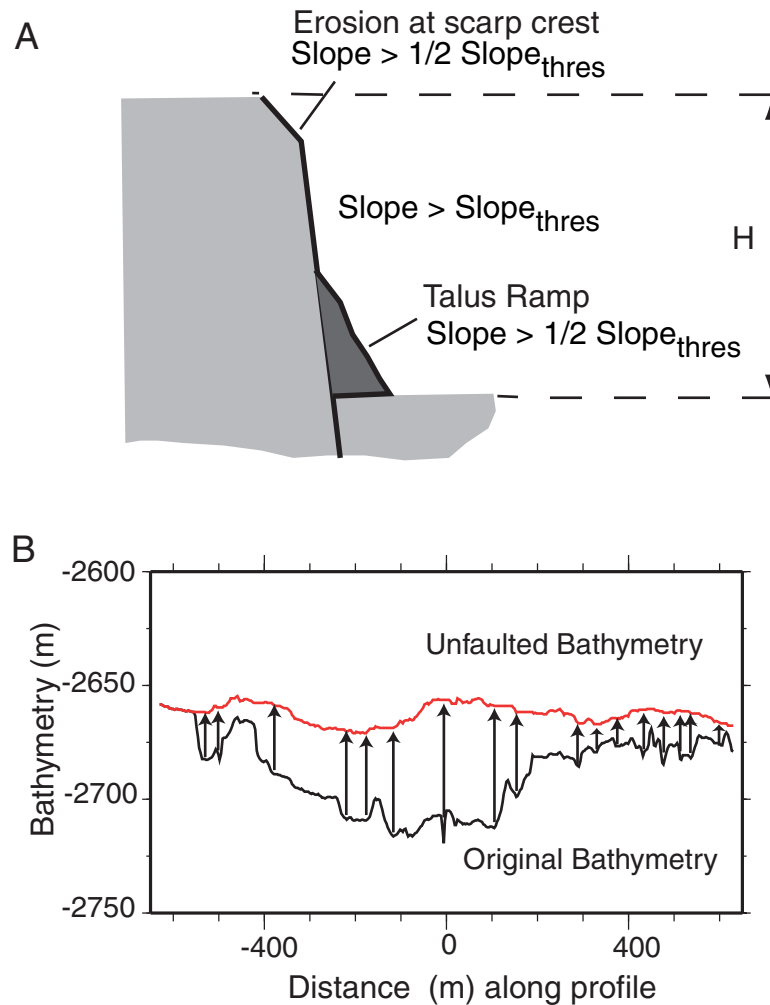


Figure 4. Schematic diagrams illustrating fault restoration procedure. (a) Vertical fault offsets (H) are calculated where bathymetric gradients exceed the input slope threshold. Lower slope regions associated with talus scarps and erosion at fault crests are included (see text). (b) The vertical fault offsets are subtracted from the original bathymetry to construct an unfaulted seafloor surface.

adjacent fault blocks are nonhorizontal and if fault dips are nonvertical. However, for the gentle regional slopes of fault blocks within the study area ($<8^\circ$) and the steep fault dips (60° to $>80^\circ$) measured with Alvin and Imagenex bathymetry for exposed portions of fault scarps, these potential errors are minor ($\sim 5\%$) [see *De Chabaliér and Avouac, 1994*].

5. Results

5.1. Vertical Displacement Fields

[17] Fault offsets measured along each bathymetric profile are gridded and displayed in map view for

both the inward- and outward-facing faults within the study area (fault facing direction is identified by position relative to the axial fissure, Figure 7). From these data, fault scarp height and fault spacing are measured for all faults longer than 50 m (Table 2). Fault spacings are measured beginning with the first fault from the axial fissure on both the east and west flanks. Fault scarp height corresponds with the average height along the length of a fault. Inward- and outward-facing scarps display similar median fault heights (9 m and 8 m) and occur in comparable numbers through the study area (20 and 18, respectively). However, the spatial distribution of inward and

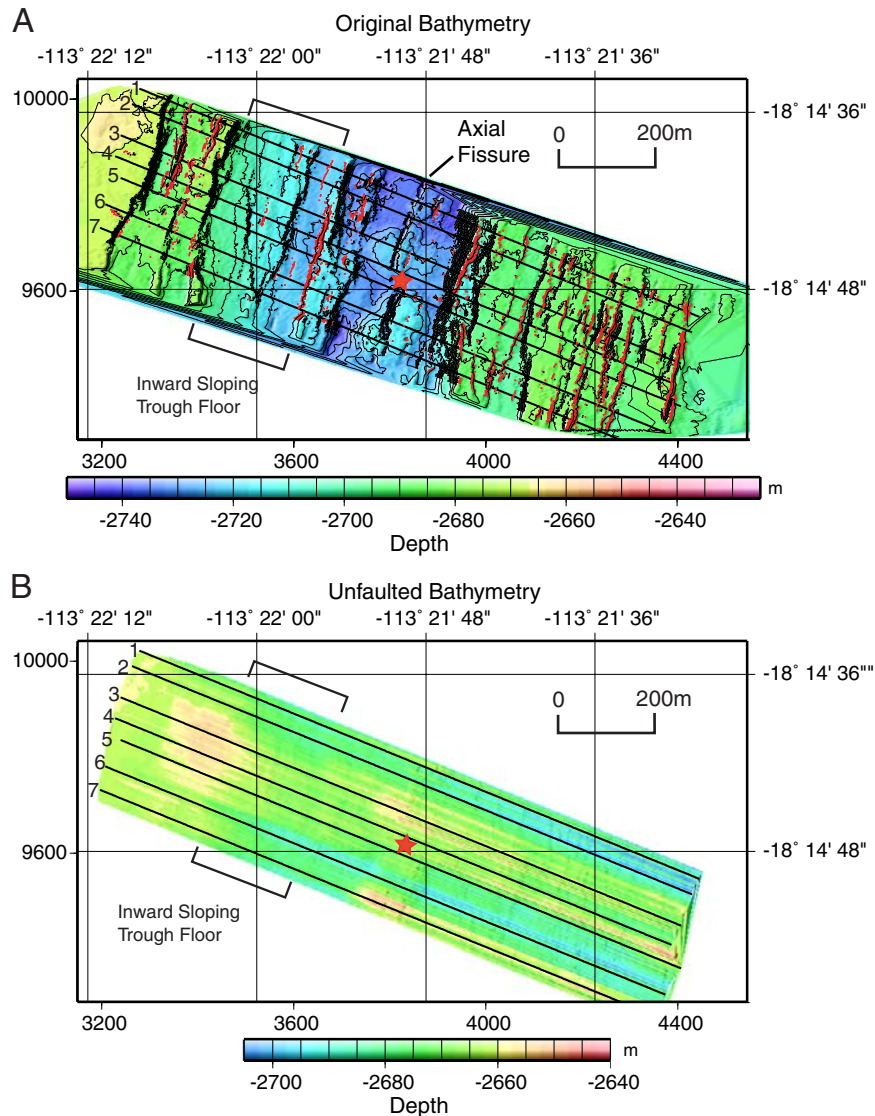


Figure 5. (a) Fault picks identified by the fault detection scheme overlain on the original bathymetry (5 m contour interval). Inward facing faults are in black and outward facing faults in red. (b) Unfaulted bathymetry calculated by removing vertical offset at each identified fault. Black numbered lines show locations of example profiles in Figure 6. Red stars show location of persistent left stepping offset at 18°14'47"S. Location of the inward sloping trough floor is indicated. Note that the color bar for Figure 5b extends over a smaller depth range than for Figure 5a.

outward faults differs, with the first outward-facing fault located further from the axial fissure, and outward faults more clustered than inward faults (Figure 7). As a result of these differences, median fault spacings are lower for the outward-facing faults (46 m compared with 70 m for inward faults) even though both fault sets occur in similar numbers.

[18] We do not measure fault length for these faults, as most are only partially imaged within

the limited north-south extent of the survey (400 m). However, visual inspection reveals that the lengths of inward and outward faults differ, with most inward-facing faults transecting the full width of the survey area, whereas the outward faults typically do not (Figure 7). Differences in cumulative vertical displacements calculated across the survey area are primarily due to these differences in fault length. Although inward- and outward-facing faults occur in similar numbers and with similar displacements, the cumulative vertical displacements are

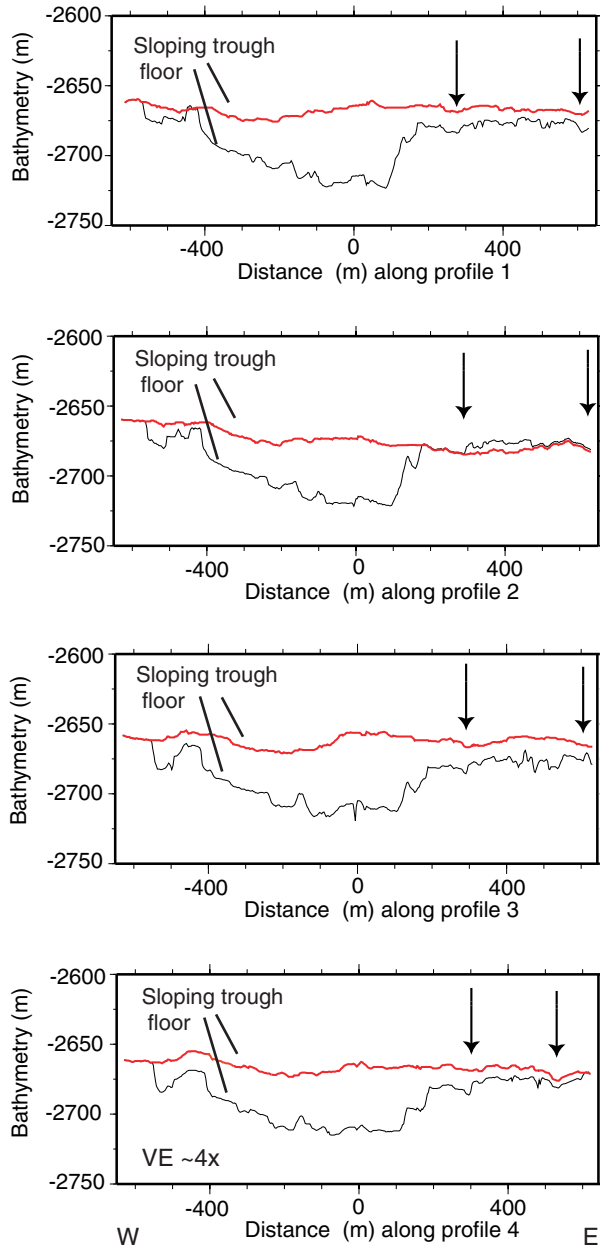


Figure 6. Example profiles showing original and unfaulted bathymetry. Profile locations are identified in Figure 5. Arrows indicate the limits of subtle undulations found on the eastern shoulder, which may correspond to individual flow lobes. The inward sloping trough floor in both the original and restored bathymetry is indicated.

roughly two-times higher for the inward-facing faults (Figures 8a–8b).

[19] The extensional strain represented by a fault population can be obtained from measurements of

cumulative fault displacement provided fault dip is known. Fault dips of 60° – 80° are measured from seafloor scarps in the study area with the lowest slopes associated with the large inward-facing faults. Fault dips measured at the seafloor may not be representative of fault dip at depth and faults may shoal with increasing depth within the crust. However, in the absence of additional constraints, we use the range of seafloor scarp dips to estimate fault strain. Spatial variations are observed in total fault strain (Figure 8c) with a humped along-axis profile indicating that fault strain through the survey area is segmented. A local minimum in the total strain profile coincides with the persistent left stepping offset located at $18^{\circ}14'47''S$ in the youngest volcanic structures and in prominent faults of the axial trough (star in Figure 8c). This strain minimum defines the boundary between two distinct segments with greater cumulative displace-

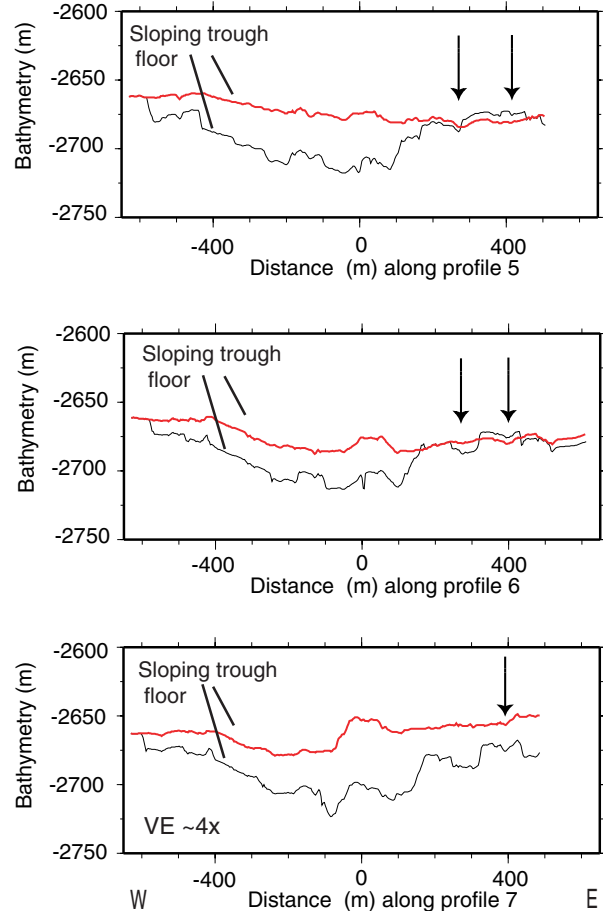


Figure 6. (continued)

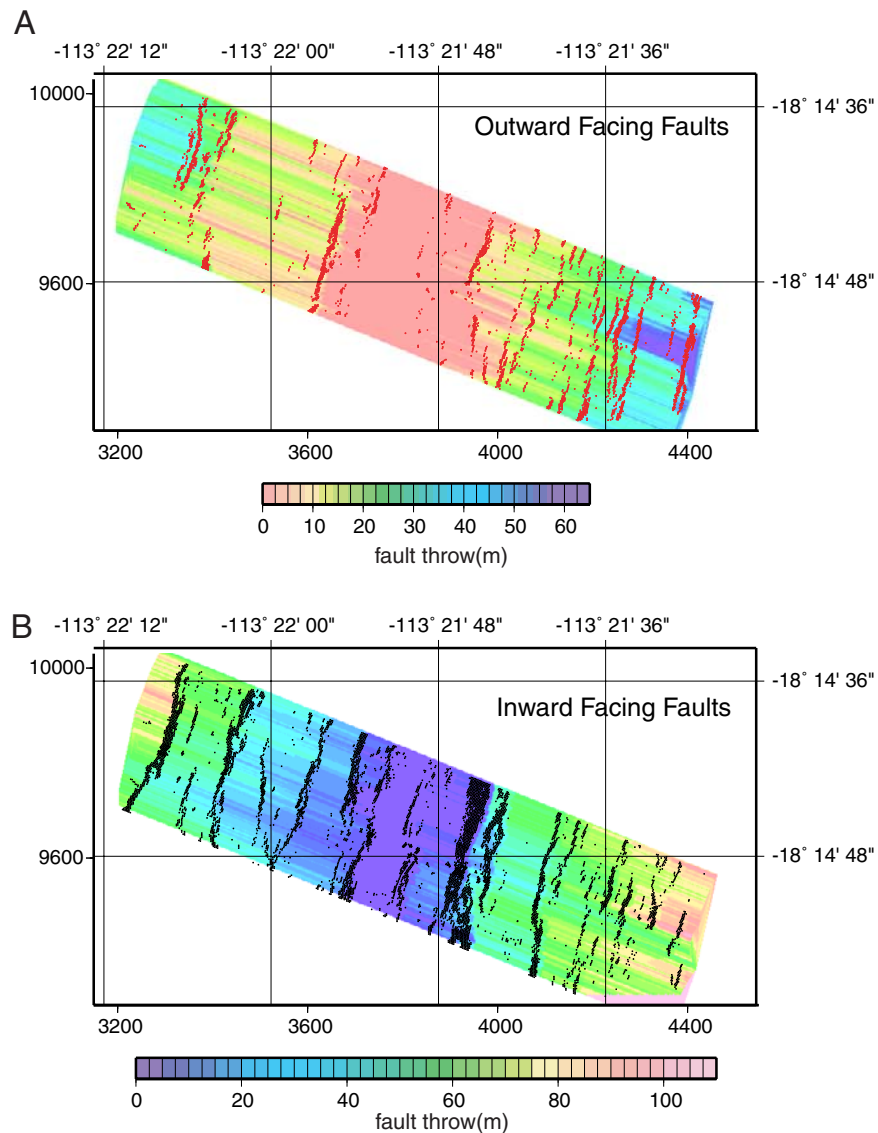


Figure 7. Vertical displacement field for (a) outward and (b) inward facing faults with fault picks from Figure 5 overlain. Offsets between fault picks and corresponding fault throw indicated by color changes occur where talus accumulations and eroded scarp crests are identified with the fault identification algorithm (see Figure 4). The two fault sets are shown with reversed color bars and different color ranges in order to emphasize the contribution of each fault set to axial bathymetry.

ments and estimated strain associated with the segment north of the 18°14'47"S offset.

5.2. Vertically Restored Seafloor

[20] Figure 5b shows the vertically restored surface obtained by gridding fault-shifted topography along each profile. Both long-wavelength (100s m) and short-wavelength (10s m) variations are observed in the restored surface. Local areas of under or over

detection of faults account for the short-wavelength noise. For example, small fault offsets will remain in the restored topography where low relief portions of faults are not adequately detected. Conversely in some locations, localized steep relief associated with data artifacts or discrete volcanic features may be flagged as fault relief. At these sites, seafloor will be shifted during the fault restoration, also contributing to the short-wavelength striping observed.

Table 2. Comparison of Fault Parameters at 18°14'S and 19°30'S

Area	Number of Faults and Percent of Total, %	Median Scarp Height, m	Quartiles ^a , m	Median Spacing, m	Quartiles ^a , m	Strain, % ^b
<i>18°14'S Axis</i>						
inward	20 (53)	9	6/18	70	42/88	7.1/1.3
outward	18 (47)	8	6/10	46	35/67	3.3/0.6
<i>19°30'S Axis and Off-Axis^c</i>						
inward	757 (39)	12	4/26	588	179/1365	1.3/0.4
outward	1196 (61)	7	3/15	294	157/693	1.2/0.35

^a Quartile values of 25% and 75% are given.

^b Average strain estimates derived from Figure 8 (calculated for 60°/80° fault dip).

^c Data from *Bohnenstiehl and Carbotte* [2001]. Fault statistics are derived from deep-tow bathymetric profiles with a vertical resolution (<1 m) comparable to that used for the axial faults at 18°14'S. Although both axial and off-axis faults are included in the 19°30'S study, the axial region comprises less than 8% of the area studied and abyssal hill faults will dominate the estimated fault properties.

[21] Long-wavelength undulations in the restored seafloor indicate the presence of consistent changes in seafloor slope over 100s of meters across the region (Figure 5b). These changes in seafloor orientation are the focus of our study and reflect the integrated effects of syn-eruption and posteruption relief forming processes (Figure 9). Syn-eruption processes include volcanic construction (Figure 9a), as well as collapse and tilting of lava flows due to flow drain out (Figure 9b), and deeper subsurface magma movements (Figure 9c). Posteruption processes include local inflation or subsidence due to subsurface magma movements that may cause seafloor tilting and/or brittle failure (Figures 9c and 9d), as well as normal faulting and block rotation (Figure 9e). Fine-scale seafloor relief will reflect the time-integrated effects of these processes which occur during the succession of dike injection and eruption events which build the upper crust. Below, we describe the primary features of the restored surface progressing from west to east across the region.

5.2.1. Western Shoulder

[22] The western trough restores to a surface that is continuous with the unfaulted western shoulder terrain and at similar shallow elevations (Figures 5b and 6). A local high rises ~15m above the surrounding flat-lying terrain and dominates the restored shoulder. This local high appears to reflect both volcanic relief associated with the lobate flows, which cover most of the western shoulder, as well as relief associated with the pillow lavas found within

the deepest portion of the western trough (Figure 3). These pillow lavas are observed within the northern part of the western trough and are associated with a west-sloping seafloor, which may reflect subsidence during or following eruption of these flows.

5.2.2. Axial Trough

[23] In the unfaulted bathymetry, the western portion of the main trough slopes gently inward toward the youngest volcanic mounds (Figures 5 and 6). This inward sag results from a 200-m-wide inclined seafloor that slopes 5° to the east. The restoration reveals that this inclined seafloor surface extends from the fissured lobates found at the base of the west wall and includes the shattered lobates and the 65–95-m-wide graben floored by sheet flows. An axis-parallel, west-facing slope located at ~113° 21'55"–57" marks the boundary of the eastward sloping seafloor. In the northern part of the study area, this boundary dips gently 8° to the west and appears to be a volcanic flow front. Further south, this boundary is an outward-facing fault scarp. In the restored surface, the pillow mounds, which comprise the youngest volcanics in the study area, rise as positive relief from the deepest portion of the axial trough.

5.2.3. Eastern Shoulder

[24] In the observed bathymetry, the eastern shoulder of the axial trough steps down toward the central depression along a series of faults scarps

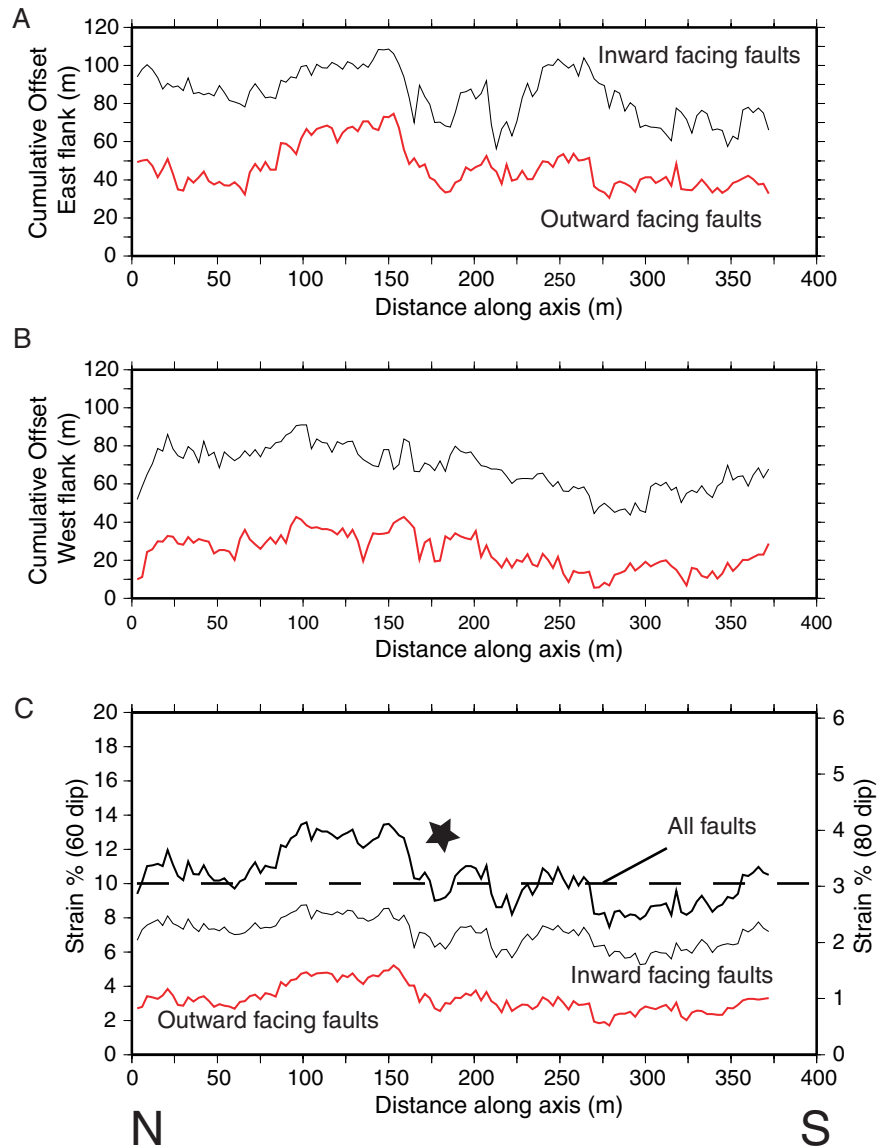


Figure 8. Cumulative fault offset plotted along axis for the (a) east flank and (b) west flank of the axis (defined relative to axial fissure) with data for inward facing faults shown in black and outward facing faults in red. (c) Total fault strain along each profile for all faults (bold black line), all inward facing (medium weight black line), and all outward facing (red line) faults. Fault strain is calculated for a fault dip of 60° (left labeled axis) and 80° (right labeled axis). Dashed line denotes 10%/3% strain. Note how cumulative displacements/strain for inward facing faults are \sim two times larger than for outward faults. Fault strain is segmented in the region with a local minimum in the total strain profiles (indicated with black star) coincident with the persistent left-stepping offset observed in the recent volcanic structures and in prominent faults of the axial trough (Figures 1 and 5). Fault strains are lower south of this left-stepping offset where a greater volume of recent volcanics are found within the innermost trough.

to form a regionally westward-sloping surface (Figures 5 and 6). However, with removal of fault offsets, the eastern shoulder restores to a gently undulating nearly horizontal surface. The undulations are correlated from profile to profile and form subtle domal forms that extend for several 10s of

meters along axis. The first undulation extends for ~ 100 m from the rim of the east wall to the first major inward-facing fault of the east shoulder. An inflection point in the restored surface occurs near this fault and a second domal form, which is 100–300 m wide, rises east of this fracture (Figure 6).

Dive observations on this shoulder are limited but reveal that these undulations are associated with lobate flows of different ages, with the flows of the first domal half form possibly contemporaneous with the lavas of the western shoulder (Figure 3). Undulations reach a maximum amplitude of 5 meters and along several profiles display a convex-up cross-section (Figure 6). These undulations are comparable in dimension and cross-sectional shape to the lobate flow mapped at 17°28'S (~600 m wide and 5–10 m thick [Sinton *et al.*, 2002;

Cormier *et al.*, 1999]) and could be similar effusive flow units.

6. Discussion

6.1. Restored Topography and Seafloor Subsidence

[25] Removal of fault offsets at 18°14'S reveals that the main crestal region of the EPR forms an asymmetric gently sagging seafloor surface and not a region of positive domal relief like that found north of 17°55'S. This asymmetric sag results from the western portion of the trough floor, which slopes 5° to the east over a distance of ~200 m, toward the current locus of magmatic activity. A variety of processes could generate this sloping seafloor surface including volcanic construction (Figure 9a), block rotation associated with faulting (Figure 9e), and subsidence associated with subsurface withdrawal (Figure 9c). A volcanic constructional origin is unlikely as this would require eruption sources to the west, opposite the lava age progression, and lava flow downhill to the east, for which there is no evidence. Block rotation associated with slip along the eastern trough wall could generate an eastward sloping trough floor. However, there is little evidence for block rotation within the inner trough, where seafloor away from the constructional pillow mounds is horizontal,

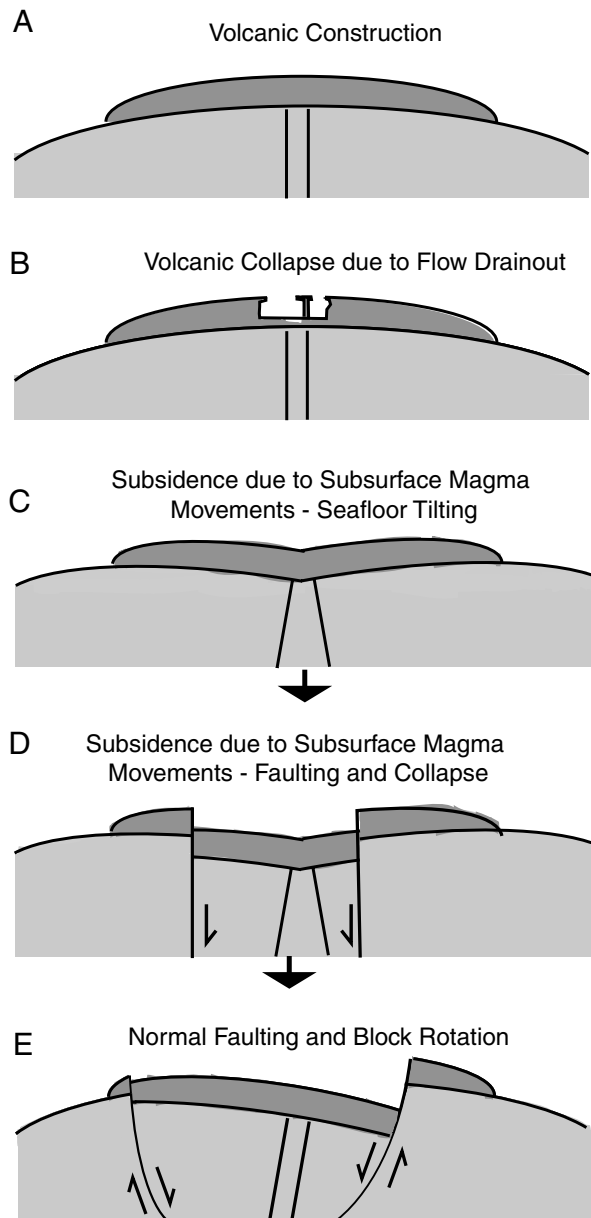


Figure 9. (opposite) Schematic representation of possible relief-forming processes within the axial neovolcanic zone and discussed within the text. (a) Volcanic construction. Emplacement of a lobate flow is shown in darker grey with associated dike. (b) Volcanic collapse due to lava flow drain out. An uncollapsed lava flow roof remnant and lava pillar is shown. (c) Surface subsidence due to subsurface magma movements. During subsidence, initially flat-lying lavas are rotated toward the center of magmatic deflation resulting in inward dipping flows while initially vertical dikes are rotated away from the center of deflation resulting in outward dipping dikes. (d) Surface subsidence due to subsurface magma movements may also give rise to brittle deformation and collapse within the axial region. (e) Block rotations associated with normal faulting on listric (shown) or planar faults will result in gently sloping fault blocks. Fine-scale seafloor relief will reflect the time-integrated effects of these magmatic and tectonic processes, which occur during the multiple dike injection and eruption events that build the upper crust.

even though the eastern trough wall has experienced recent fault motion as indicated by sediment free talus (Figures 1b and 3).

[26] Our preferred interpretation is that the western portion of the trough floor was tilted during subsidence associated with subsurface magmatic movements. Subsidence associated with magmatic deflation is well established in terrestrial volcanic systems where ground deformation studies document both rapid subsidence events during volcanic eruptions as well as longer term gradual subsidence within quiet periods between eruptions [e.g., Tryggvason, 1994; Rymer *et al.*, 1997; Sturkell and Sigmundsson, 2000]. These surface deflations are attributed either to magma withdrawal or to the solidification and cooling of magma within the subsurface magma source. Subsidence associated with a submarine eruption event has been reported for the 1998 eruption at Axial Volcano [Fox *et al.*, 2001]. During the Axial eruption, subsidence was recorded for 5 days following the main inflation/deflation phase of the event by a tiltmeter embedded within the flow and fortuitously functioning throughout the eruption. The sheet flow that was emplaced during this event collapsed by up to 6 m in its interior, with the downslope of the collapsed area directed toward the eruption source. By analogy with these observations at Axial Volcano and other terrestrial volcanoes, we attribute the inward-sloping trough floor at $18^{\circ}14'S$ to subsidence associated with magmatic deflation.

[27] There is growing evidence that inward-dipping lavas are a common feature of the internal structure of the extrusive layer of oceanic crust. Axis-dipping lavas are well known within the lava pile in Iceland [e.g., Palmason, 1980] and have long been proposed based on models of crustal accretion [e.g., Cann, 1974]. Recent studies of paleomagnetic inclinations within drill cores indicate axis-tilted lavas [Schouten and Denham, 2000] and new visual observations of tectonic exposures at Hess Deep and the Blanco Fracture Zone reveal that axis-dipping flows are pervasive within the lava section [Karson *et al.*, 2002]. Rotations of lava flows from their orientation at emplacement are well established from paleomagnetic data and were originally attributed to block rotations associated with abyssal

hill faulting (Figure 9e) [e.g., Verosub and Moores, 1981]. More recent studies have emphasized the potential importance of flow rotation due to progressive lava burial as the volcanic layer thickens within a narrow axial zone [e.g., Schouten and Denham, 2000]. However, seafloor subsidence due to subsurface magma movements (e.g., Figure 9c), as observed at Axial Volcano and inferred in our study, provides a mechanism for dipping lavas to develop *prior to*, as well as during, lava burial. Direct observations at Hess Deep reveal intense brittle deformation within the dike and lava section, 30° – 50° dipping flows within the lower lavas, and outward rotated dikes, which Karson *et al.* [2002] attribute to subsidence and caldera collapse within the axial region. Positive confirmation of magmatic subsidence within the axial region at $18^{\circ}14'S$ will require further studies such as paleomagnetic observations of oriented drilled samples of the volcanic section, tiltmeter measurements, and study of lava flow direction indicators.

6.2. Axial Fault Population and Ridge Crest Subsidence

[28] Near-bottom studies of the EPR axis reveal that within the innermost 1–2 km, fissures are the dominant tectonic structures and the primary fractures with significant vertical offset are the walls of the axial summit trough [e.g., Choukroune *et al.*, 1984; Crane, 1987; Bicknell *et al.*, 1987; Wright *et al.*, 1995]. The large-scale normal faults that bound the abyssal hills are believed to develop a few kilometers from the axis due to changing stress conditions as crust moves away from the axial magma chamber and beyond the zone of active dike injection [e.g., Bicknell *et al.*, 1987; Edwards *et al.*, 1991; Goff, 1991; Carbotte and Macdonald, 1994a].

[29] Within the axial region at $18^{\circ}14'S$ a dense population of faults is present, raising the possibility that abyssal hill faults may indeed originate at the ridge crest during axial trough development. In this scenario, fault parameters for abyssal hill faults and ridge-axis fault populations should be similar. Although no high resolution bathymetric data are available for abyssal hill faults at $18^{\circ}14'S$, fault parameters for the ridge flanks are available from a nearby study at $19^{\circ}30'S$ (Table 2) [Bohnenstiehl

and Carbotte, 2001]. Regional bathymetry data suggest that the ridge flanks at 19°30'S are more tectonized than at 18°14'S and fault parameters may differ between these two areas (with somewhat larger fault throws and smaller spacings expected at 19°30'S). However, bathymetric data used in both studies are of similar high resolution (sub meter) and meaningful comparisons of fault parameters can be made.

[30] Median fault heights measured for the axial region at 18°14'S are very similar to those measured for the abyssal hill faults at 19°30'S (Table 2). However, the axial fault population is distinct from the ridge flank faults in a number of important characteristics. Fault spacings are an order of magnitude lower for the ridge axis faults (median values of 70/46 m compared with 588/294 m, Table 2). The extensional strain represented by these faults is strongly dependent on fault dip for which there is little information at the EPR. Assuming the same range of fault dips measured in this study (60°–80°) for both the axial and off-axis faults, the total extensional strain represented by the axial fault population (10%–2%) is 3–4 times greater than that of the off-axis faults (2.5%–0.75%, estimated from *Bohnenstiehl and Carbotte* [2001] for 60° and 80° fault dips, Table 2). These differences represent maximum likely differences as newly formed, ridge-axis faults may be systematically steeper than off-axis faults (i.e., fault dips may evolve with ongoing slip and fault propagation deeper within the crust).

[31] Although inward- and outward-facing faults occur in comparable numbers in the axial region, the total extensional strain associated with the inward faults is roughly twice that of the outward faults. In contrast, inward-facing faults on the ridge flanks are typically less abundant than outward faults, and both populations accommodate similar strains (Table 2). Furthermore, outward-facing faults on the ridge flanks commonly occur in packets of small throw closely spaced faults, antithetic to large inward faults [*Carbotte and Macdonald*, 1994b; *Bohnenstiehl and Carbotte*, 2001]. This pattern is attributed to failure in the hanging walls of large “master” inward-facing faults, which flatten with depth. In the axial region at 18°14'S,

little evidence for this pattern is found, and fractures predominantly form graben structures.

[32] From these differences in the abundance and distribution of faults on- and off-axis, we infer that the abyssal troughs and hills found on the ridge flanks are not frozen structures inherited from fault-bounded axial troughs like that at 18°14'S. The axial faults cannot evolve into ridge flank faults without significant modification, presumably via volcanic burial as seafloor is transported through the plate boundary zone [e.g., *Macdonald et al.*, 1996; *Carbotte et al.*, 1997]. Furthermore, the small fault spacings observed in the axial region suggests that these fractures correspond with fissures that have undergone vertical offset after their formation. In an evolving fault or fissure population, stress shadowing is expected to occur such that new fractures cannot develop within the stress shadow of nearby faults [e.g., *Nur*, 1982; *Melosh and Williams*, 1989]. As faults evolve, some will continue to grow and deepen while nearby fractures cease to develop [e.g., *Cowie*, 1998]. The width of the stress shadow is approximately equal to fracture depth, and the closely spaced faults observed at 18°14'S (median spacings of 70 m and 46 m) indicate that these fractures likely originated as shallow fissures. We suggest that the vertical relief associated with these fractures reflects subsidence of the crestal region associated with magma withdrawal from the underlying magma reservoir during the eruption events that build the upper crust (e.g., Figure 9d). With multiple subsidence events associated with magmatic activity throughout the evolution of the trough, these fractures grow in size and accumulate throw. The fault population present at the ridge crest could represent an analog for the zones of dense brittle deformation observed within the lower lavas and dike section along fault exposures at Hess Deep [*Karson et al.*, 2002]. With volcanic burial as seafloor is transported out of the axial region, the dense fault population and extensive brittle deformation now present at 18°14'S will become part of the internal architecture of the upper crust.

6.3. Magmatic Deflation

[33] From the vertical deformation field shown in Figure 7, we estimate the volume of surface sub-

Table 3. Comparison of Subsidence Volumes with Crustal Volumes

Feature	Volume of Subsidence, ^a m ³	ΔV_{magma} , ^{a,b} m ³	ΔV_{magma} ^{a,c} m ³	Width of Subsidence Zone, m	Volume of Underlying Upper (Whole) Crust, ^{a,d} m ³	Percentage of Upper (Whole) Crustal Volume Represented by Surface Subsidence
Main trough	25–35 × 10 ⁶	25–35 10 ⁶	31–44 × 10 ⁶	600	8.4 × 10 ⁸ (36 × 10 ⁸)	3–4% (0.7–1%)

^a Volume estimates are for 1-km length of ridge.

^b Calculated for incompressible magma assuming a horizontal sill-like source ($\Delta V_{\text{chamber}} = \Delta V_{\text{magma}}$).

^c Calculated for compressible magma assuming a horizontal sill-like source ($\Delta V_{\text{chamber}} = 1.25\Delta V_{\text{magma}}$).

^d Calculated assuming a crustal thickness of 6 km.

subsidence represented by the main trough at 18°14'S (Table 3). Elastic models for magma chamber inflation and deflation predict a direct relationship between surface subsidence and the volume change within the magma reservoir [e.g., *Mogi*, 1958]. For a sill-like magma body the surface subsidence or uplift (ΔV_{ed}) is related to the volume change within the source magma chamber (ΔV_{ch}) by,

$$\Delta V_{\text{ed}}/\Delta V_{\text{ch}} = 1 - (1 - 2\nu)\sin^2\delta/2$$

where δ is the dip of the sill and ν is Poisson's ratio [*Delaney and McTigue*, 1994]. For a horizontal body, $\delta = 0^\circ$ and the volume change of the magma reservoir, ΔV_{ch} , equals the volume of subsidence or uplift, ΔV_{ed} . For the case of incompressible magmas, ΔV_{ch} will equal the volume of magma withdrawn from or injected into the magma chamber (ΔV_{magma}). However, for a compressible magma with significant dissolved gas content, bulk expansion (compression) of the remaining magma occurs during magma withdrawal from (injection into) the source reservoir and ΔV_{ch} provides only a minimum estimate of ΔV_{magma} [*Johnson et al.*, 2000]. From gravity and ground motion observations at Kilauea, magma withdrawal to surface subsidence ratios ($\Delta V_{\text{magma}}/\Delta V_{\text{ed}}$) of ~ 3.3 are inferred for highly compressible magmas with high CO₂ contents whereas ratios of 1.25 to 1.0 are derived for magmas of low compressibility [*Johnson*, 1992; *Johnson et al.*, 2000].

[34] Assuming low gas contents for southern EPR magmas, we use the surface subsidence represented by the main trough at 18°14'S to estimate

magma withdrawal volumes using the relation for magmas of low compressibility from Kilauea (Table 3). These values provide estimates of ΔV_{magma} of 25 to 44 × 10⁶ m³, calculated for a one kilometer length of ridge (Table 3). *Sinton et al.* [2002] report average size eruption volumes of 10–50 × 10⁶ m³ for this region. Eruptive fissures associated with these lava flows vary from <1 to 18 km in length and these eruptions may tap a comparable length of the magma source region. Assuming, for example, a 10 km length of the magma source region is tapped during a typical eruption, the surface subsidence volumes at 18°14'S, correspond with magma withdrawal volumes associated with from 5 to 44 eruptions of the size range reported by *Sinton et al.* [2002]. If intrusion of a 1-m-wide dike from a magma source at 1–1.4 km depth [e.g., *Hoofst et al.*, 1997] is associated with each eruption event, an additional intrusive volume of 10–14 × 10⁶ m³ will be emplaced. Hence, subsidence volumes represented by the axial trough at 18°14'S may correspond with 4–22 intrusive/eruptive events of typical size along the EPR.

[35] There is considerable debate regarding the nature of the magmatic system feeding the lower crust at the EPR [*Phipps Morgan and Chen*, 1993; *Keleman et al.*, 1997]. However, the magma reservoir for the upper crust, including the dike and lava sections, is widely believed to be the axial magma lens imaged in reflection seismic studies [e.g., *Sinton and Detrick*, 1992]. Assuming the subsidence represented by the axial trough at 18°14'S reflects magma withdrawal from the crustal magma lens and not from magma movements within the underlying

crystal mush zone, we can relate the volume of surface subsidence to the volume of this lens. For a range of lens thicknesses of 20–100 m [Vera *et al.*, 1990; Hussenoeder *et al.*, 1996] and width of 590 m in this region [Hooft *et al.*, 1997], the axial magma lens volume per kilometer of ridge crest is $12\text{--}59 \times 10^6 \text{ m}^3$. The volume subsidence represented by the main trough is 50–300% of estimated magma lens volumes. Hence, the subsidence represented by the trough could be created in complete withdrawal of magma from up to 3 magma lenses of typical dimensions during the evolution of the trough.

[36] The time period over which subsidence occurred in this region is an important question which, in the absence of dated lava samples, is difficult to establish. We assume a maximum age for the observed subsidence is provided by the estimated age of lavas on the trough shoulders of 3000–4000 years (see section 3.3). A minimum duration for the axial subsidence is more difficult to constrain. Alvin dive observations reveal that lavas are not of uniform age within the axial trough, but rather they young toward the deepest portion which includes the inner trough floor and axial pillow mounds. Lava pillars are observed within the narrow graben floored by sheet flows located just west of the inner trough. These are delicate structures unlikely to survive large scale vertical motion, and we infer that these lavas must have been emplaced after the main stage of tectonic deformation forming the axial trough. The presence of exposed talus piles at the base of all faults of the axial trough indicate tectonic activity after lava emplacement. However, an age progression in tectonic activity is evident from the extent of sediment cover on talus accumulations at the base of faults within the trough, with unsedimented talus (hence recent faulting) found only at the base of the inner trough walls. Based on these relationships we infer that at minimum, the inner trough has formed since subsidence initiated and assume the spreading age of the inner trough (~ 1430 years) provides a minimum duration of axial subsidence.

[37] For spreading rates of 140 mm/yr, we can estimate the number of extrusive and intrusive events required to build the upper crust during this estimated period of axial trough development

(1430–4000 years). Within 4000 years of spreading, 56–280 eruption events are needed to build an extrusive layer 500 m thick over a 10-km-length of ridge with typical size eruptive volumes of $10\text{--}50 \times 10^6 \text{ m}^3$. Over this same time period, 560 dike injection events are required to build a 1-km-thick dike section from 1-meter-wide dikes. For 1430 years of spreading, 20–102 eruptions and 200 dike injection events are needed. The number of volcanic events estimated from the subsidence volumes of the axial trough at $18^\circ 14'S$ (4–22) correspond with only a small subset of the total number of events required to build the upper crust during the estimated period of axial subsidence.

[38] In Table 3 the volume of surface subsidence estimated from the vertical displacement field at $18^\circ 14'S$ is compared to the volume of the underlying crustal section. For an upper crustal lid above a magma sill located at a depth of 1.4 km (estimated from Hooft *et al.* [1997]), the seafloor subsidence volumes are only a small fraction (3–4%) of the associated upper crustal sections (Table 3). These surface subsidence volumes are a measure of the mismatch between the volume of magma which must be resupplied to the magma lens in order to keep pace with ongoing plate separation. The small mismatch of 3–4% measured at $18^\circ 14'S$ indicates that only a very small deficiency in magma recharge to the lens is needed to create the axial depression present at $18^\circ 14'S$. Models which invoke changes in axial thermal structure or a marked reduction in magma supply associated with a waxing/waning magmatic cycle, are not required to account for the pronounced axial trough present in this region. We envision that the seafloor subsidence represented by the axial trough reflects the cumulative effects of magma withdrawal events from the crustal magma reservoir associated with typical sized eruptions as the trough evolves. This model builds upon the caldera collapse model of numerous previous researchers [e.g., Lonsdale, 1977; Kappel and Ryan, 1986; Macdonald and Fox, 1988; Lagabriele and Cormier, 1999] and emphasizes the development of an axial trough due to subsidence events associated with a small subset of the frequent dike injection and volcanic eruption events which build the upper

crust in a system where magma resupply and discharge do not always keep pace.

6.4. Linked Tectonic and Volcanic Structures

[39] At 18°14'S, a close coincidence is present between the fine-scale segmentation of volcanic features and tectonic structures of the axial trough. A left-stepping offset of <100 m is observed at 18°14'47''S in the axial fissure, the pillow domes associated with the youngest volcanism, the faults bounding the inner trough, and within the western trough. Although lateral jogs at this location are not observed for all faults within the axial trough, those fractures without segmentation are small throw structures, presumably of limited depth extent within the shallow upper crust. Segmentation in total tectonic strain is also observed within the study area, coincident with the location of this persistent left-stepping offset. The lower tectonic strain measured for the segment south of the jog is associated with the larger of the two pillow dome structures and hence a greater volume of recent volcanics. It appears that reduced tectonic strain may be balanced by greater magmatism within this area.

[40] Close linkage between the geometry of tectonic and volcanic structures of the axial trough at 18°14'S may be a direct result of brittle failure in response to subsidence associated with magmatic events. In other areas along the EPR, segmentation is observed in the midcrustal magma lens coincident with the fine-scale segmentation of the axial summit trough [Babcock *et al.*, 1998; Carbotte *et al.*, 2000]. The linkage between offsets in seafloor structures of only a few 100s of meters with segmentation of the magma lens located 1–1.5 km below the seafloor suggests a genetic connection. The development of the axial summit trough via subsidence in response to withdrawal events from the crustal magma reservoir provides a mechanism for this close correspondence.

7. Summary

[41] Our analysis of ultra-high-resolution bathymetry data from the EPR at 18°14'S suggests that seafloor subsidence due to magmatic deflation

accounts for the pronounced axial depression found in this region. A detailed vertical displacement field is derived from the bathymetry and used to characterize the axial fault population present in the region. Removal of this displacement field from the original bathymetry reveals a gently inward sloping surface coincident with the western portion of the axial trough. We attribute this sloping seafloor to subsidence associated with magma withdrawal within the underlying magma source region. The axial faults present at 18°14'S are comparable in height to abyssal hill faults found on the flanks of the southern EPR. However, fault spacings are an order of magnitude lower and the extensional strain represented by these faults is roughly 3–4 times higher than is measured for ridge flank fault populations. These differences indicate the axial fault population cannot be rafted onto the ridge flanks to form abyssal hill faults without significant modification, presumably via volcanic burial. We suggest the axial faults correspond with a fissure population that has experienced significant vertical offset due to seafloor subsidence. With volcanic burial, the extensive brittle deformation and collapse now observed at 18°14'S will become part of the internal architecture of the upper crust. The volume of the surface subsidence represented by the axial topography is only a small fraction (3–4%) of the underlying upper crustal section. The small size of these subsidence volumes relative to the underlying upper crustal sections suggests that only a small deficiency in the rate of magma recharge of the axial magma lens relative to withdrawal could create the axial trough. Hence, a significant change in axial thermal structure or a sustained reduction in magma volumes within the crustal magma reservoir is not required to account for the pronounced axial trough present in this region.

Acknowledgments

[42] This research was supported by NSF grant OCE 97-11790 to S. M. Carbotte and W. B. F. Ryan. We thank Delwayne Bohnstiehl, Roger Buck, Dan Scheirer and Associated Editor Don Forsyth and for their careful reviews which improved the manuscript. Bathymetric data used in this study were collected under OCE-9730813 to M.-H. Cormier and W. B. F. Ryan. Dive observations and sample collection were supported by NSF grant OCE 96-3398 to J. Sinton. This is Lamont-Doherty Earth Observatory contribution number 6383.

References

- Alexander, R. T., and K. C. Macdonald, Sea Beam, SeaMARC II and ALVIN-based studies of faulting on the East Pacific Rise 9°20'N–9°50'N, *Mar. Geophys. Res.*, *18*, 557–587, 1996.
- Auzende, J.-M., et al., Recent tectonic, magmatic and hydrothermal activity on the East Pacific Rise between 17° and 19°S: Submersible observations, *J. Geophys. Res.*, *101*, 17,995–18,010, 1996.
- Babcock, J. M., A. J. Harding, G. M. Kent, and J. A. Orcutt, An examination of along-axis variation of magma chamber width and crustal structure on the East Pacific Rise between 13°30'N and 12°20'N, *J. Geophys. Res.*, *103*, 30,451–30,467, 1998.
- Bicknell, J. D., J. C. Sempere, K. C. Macdonald, and P. J. Fox, Tectonics of a fast spreading center: A deep-tow and sea beam survey on the East Pacific Rise at 19°S, *Mar. Geophys. Res.*, *9*, 25–45, 1987.
- Bohnenstiehl, D. R., and S. M. Carbotte, Faulting patterns near 19°30'S on the East Pacific Rise: Fault formation and growth at a superfast-spreading center, *Geochem. Geophys. Geosyst.*, *2*, paper number 2001GC000156, 2001.
- Cann, J. R., A model for oceanic crustal structure developed, *Geophys. J. R. Astron. Soc.*, *39*, 169–187, 1974.
- Carbotte, S. M., and K. C. Macdonald, The axial topographic high at intermediate and fast spreading ridges, *Earth Planet. Sci. Lett.*, *128*, 85–97, 1994a.
- Carbotte, S. M., and K. C. Macdonald, Comparison of seafloor tectonic fabric at intermediate, fast, and super fast spreading ridges: Influence of spreading rate, plate motions, and ridge segmentation on fault patterns, *J. Geophys. Res.*, *99*, 13,609–13,633, 1994b.
- Carbotte, S. M., J. C. Mutter, and L. Xu, Contribution of tectonism and volcanism to axial and flank morphology of the southern EPR from a study of Layer 2A geometry, *J. Geophys. Res.*, *102*, 10,165–10,184, 1997.
- Carbotte, S. M., G. Ponce-Correa, and A. Solomon, Evaluation of morphological indicators of magma supply and segmentation from a seismic reflection study of the EPR 15°30'–17°N, *J. Geophys. Res.*, *105*, 2737–2759, 2000.
- Choukroune, P., J. Francheteau, and R. Hekinian, Tectonics of the East Pacific Rise near 12°50'N: A submersible study, *Earth Planet. Sci. Lett.*, *68*, 115–127, 1984.
- Cormier, M. H., D. Scheirer, K. Macdonald, S. White, and R. Haymon, Sojourn Leg 1: Detailed study of asymmetries about the East Pacific Rise, 15°30'–20°S, RIDGE Events *8.2*, 1–5, 1997.
- Cormier, M.-H., W. B. F. Ryan, W. Jin, A. Shah, A. M. Bradley, D. R. Yoerger, H. Singh, J. Sinton, R. Batiza, and K. Rubin, Building of the extrusive crust of the EPR at 17°28'S through fissure-fed inflationary lava flows, *Eos Trans. AGU*, *80*, F1097, 1999.
- Cowie, P. A., Normal fault growth in three-dimensions in continental and oceanic crust, in *Faulting and Magmatism at Mid-Ocean Ridges*, *AGU Monogr.*, edited by W. R. Buck, P. T. Delaney, J. A. Karson, and Y. Lagabriele, pp. 325–348, AGU, Washington, D. C., 1998.
- Crane, K., Structural evolution of the East Pacific Rise axis from 13°10'N to 10°35'N: Interpretations from SeaMARC I data, *Tectonophysics*, *136*, 65–124, 1987.
- De Chabaliere, J.-B., and J.-P. Avouac, Kinematics of the Asal Rift (Djibouti) determined from the deformation of Fieale volcano, *Science*, *265*, 1677–1681, 1994.
- Dekov, V. M., and V. M. Kuptsov, Late Quaternary rates of accumulation of metal-bearing sediments on the East Pacific Rise, *Oceanology*, *32*, 94–101, 1992.
- Delaney, P. T., and D. F. McTigue, Volume of magma accumulation or withdrawal estimated from surface uplift or subsidence with application to the 1960 collapse of Kilauea Volcano, *Bull. Volcanol.*, *56*, 417–424, 1994.
- Edwards, M. H., D. J. Fornari, J. A. Madsen, A. Malinverno, and W. B. F. Ryan, Evaluating plate tectonic predictions using SeaMARC II data for the East Pacific Rise, *J. Geophys. Res.*, *96*, 7995–8017, 1991.
- Fornari, D. J., R. M. Haymon, M. R. Perfit, T. K. P. Gregg, and M. H. Edwards, Axial summit trough of the East Pacific Rise 9°–10°N: Geological characteristics and evolution of the axial zone on fast spreading mid-ocean ridges, *J. Geophys. Res.*, *103*, 9827–9855, 1998.
- Fox, C. G., W. W. Chadwick Jr., and R. W. Embley, Seafloor instrument caught in lava flow gives new insight into submarine eruptions, *Nature*, *412*, 727–729, 2001.
- Gregg, T. K. P., and W. W. Chadwick Jr., Submarine lava-flow inflation: A model for the formation of lava pillars, *Geology*, *24*, 981–984, 1996.
- Goff, J. A., A global and regional stochastic analysis of near-ridge abyssal hill morphology, *J. Geophys. Res.*, *96*, 21,713–21,737, 1991.
- Goff, J. A., and M. C. Kleinrock, Quantitative comparison of bathymetric survey systems, *Geophys. Res. Lett.*, *18*, 1243–1256, 1991.
- Haymon, R. M., et al., Distribution of fine-scale hydrothermal, volcanic and tectonic features along the EPR crest, 17°15'–18°30'S: Results of near bottom acoustic and optical surveys, *EOS Trans. AGU*, *78*(46), F705, Fall Meet. Suppl., 1997.
- Hooff, E. E., R. S. Detrick, and G. M. Kent, Seismic structure and indicators of magma budget along the southern East Pacific Rise, *J. Geophys. Res.*, *102*, 27,319–27,340, 1997.
- Hussenoeder, S. A., J. A. Collins, G. M. Kent, and R. S. Detrick, Seismic analysis of the axial magma chamber reflector along the southern East Pacific Rise from conventional seismic reflection profiling, *J. Geophys. Res.*, *101*, 22,087–22,105, 1996.
- Johnson, D. J., Dynamics of magma storage in the summit reservoir of Kilauea Volcano, Hawaii, *J. Geophys. Res.*, *97*, 1807–1820, 1992.
- Johnson, D. J., F. Sigmundsson, and P. T. Delaney, Comment on “Volume of magma accumulation or withdrawal estimated from surface uplift or subsidence with application to the 1960 collapse of Kilauea Volcano”, *Bull. Volcanol.*, *61*, 491–493, 1960.
- Kappel, E. S., and W. B. F. Ryan, Volcanic episodicity and a non-steady state rift valley along the northeast Pacific spreading centers: Evidence from SeaMARC I, *J. Geophys. Res.*, *91*, 13,925–13,940, 1986.

- Karson, J. A., E. M. Klein, S. D. Hurst, C. E. Lee, P. A. Rivizzigno, D. Curewitz, and A. R. Morris, Structure of uppermost fast-spread oceanic crust exposed at the Hess Deep Rift: Implications for subaxial processes at the East Pacific Rise, *Geochem. Geophys. Geosyst.*, *3*(1), 1002, doi:10.1029/2001GC000155, 2002.
- Keleman, P. B., K. Koga, and N. Shimizu, Geochemistry of gabbro sills in the crust-mantle transition of the Oman ophiolite: Implications for the origin of the lower crust, *Earth Planet. Sci. Lett.*, *146*, 475–488, 1997.
- Kleinrock, M. C., R. N. Hey, and A. E. Theberge Jr., Practical geological comparison of some seafloor survey instruments, *Geophys. Res. Lett.*, *19*, 1407–1410, 1992.
- Lagabrielle, Y., and M.-H. Cormier, Formation of large summit troughs along the East Pacific Rise as collapse calderas: An evolutionary model, *J. Geophys. Res.*, *104*, 12,971–12,988, 1999.
- Lonsdale, P., Structural geomorphology of a fast spreading rise crest: The East Pacific Rise near 3°25'S, *Mar. Geophys. Res.*, *3*, 251–293, 1977.
- Macdonald, K. C., and P. J. Fox, Axial summit graben and cross-sectional shape of the East Pacific Rise as indicators of axial magma chambers and recent volcanic eruptions, *Earth Planet. Sci. Lett.*, *88*, 119–131, 1988.
- Macdonald, K. C., P. J. Fox, R. T. Alexander, R. Pockalny, and P. Gente, Volcanic growth faults and the origin of Pacific abyssal hills, *Nature*, *380*, 125–129, 1996.
- Marchig, V., J. Erzinger, and P.-M. Heinze, Sediment in the black smoker area of the East Pacific Rise (18.5°S), *Earth Planet. Sci. Lett.*, *79*, 93–106, 1986.
- Melosh, H. J., and C. A. Williams Jr., Mechanics of graben formation in crustal rocks: A finite element analysis, *J. Geophys. Res.*, *94*, 13,961–13,973, 1989.
- Mogi, K., Relations between eruptions of various volcanoes and the deformations of the ground surfaces around them, *Bull. Earthquake Res. Inst. Univ. Tokyo*, *36*, 99–134, 1958.
- Nur, A., The origin of tensile fracture lineaments, *J. Struct. Geol.*, *4*, 31–40, 1982.
- Pálmason, G., A continuum model of crustal generation in Iceland, *J. Geophys.*, *47*, 7–18, 1980.
- Phipps Morgan, J., and Y. J. Chen, The genesis of oceanic crust: Magma injection, hydrothermal circulation, and crustal flow, *J. Geophys. Res.*, *98*, 6283–6298, 1993.
- Rymer, H., J. Cassidy, C. A. Locke, and F. Sigmundsson, Post-eruptive gravity changes from 1990 to 1996 at Krafla volcano, Iceland, *J. Volcanol. Geotherm. Res.*, *87*, 141–149, 1997.
- Scheirer, D. S., D. J. Fornari, S. E. Humphris, and S. Lerner, High-resolution seafloor mapping using the DSL-120 sonar system: Quantitative assessment of sidescan and phase-bathymetry data from the Lucky Strike segment of the Mid-Atlantic Ridge, *Mar. Geophys. Res.*, *21*, 121–142, 2000.
- Schouten, H., and C. R. Denham, Comparison of volcanic construction in the Troodos ophiolite and oceanic crust using paleomagnetic inclinations from Cyprus Crustal Study project (CCSP) CY-1 and CY-1A and Ocean Drilling Program (ODP) 504B drill cores, in *Ophiolites and Oceanic Crust: New Insights from Field Studies and the Ocean Drilling Program: Boulder, Colorado, Geol. Soc. Am. Spec. Pap. 349*, edited by Y. Dilek, E. M. Moores, D. Elthon, and A. Nicolas, pp. 181–194, 2000.
- Shah, A., M. Cormier, W. Ryan, W. Jin, J. Sinton, E. Bergmanis, J. Carlut, A. Bradley, and D. Yoerger, Episodic dike swarms inferred from near-bottom magnetic anomaly maps at the southern East Pacific Rise, *J. Geophys. Res.*, *107*, doi:10.1029/2001JB000564, in press, 2002.
- Sinton, J., E. Bergmanis, K. Rubin, R. Batiza, T. K. P. Gregg, K. Gronvold, K. Macdonald, and S. White, Volcanic eruptions on mid-ocean ridges: New evidence from the superfast spreading East Pacific Rise, 17°–9°S, *J. Geophys. Res.*, *107*(B6), 2115, doi:10.1029/2000JB000090, 2002.
- Sinton, J. M., and R. S. Detrick, Mid-ocean ridge magma chambers, *J. Geophys. Res.*, *97*, 197–216, 1992.
- Sinton, J. M., S. M. Smaglik, J. J. Mahoney, and K. C. Macdonald, Magmatic processes at superfast Mid-Ocean Ridges: Glass compositional variations along the East-Pacific Rise 13°–23°S, *J. Geophys. Res.*, *96*, 6133–6155, 1991.
- Sturkell, E., and F. Sigmundsson, Continuous deflation of the Askja caldera, Iceland, during the 1983–1998 eruptive period, *J. Geophys. Res.*, *105*, 25,671–25,684, 2000.
- Tryggvason, E., Observed ground deformation at Hekla, Iceland prior to and during the eruptions of 1970, 1980–1981 and 1991, *J. Volcanol. Geotherm. Res.*, *61*, 281–291, 1994.
- Vera, E. E., J. C. Mutter, P. Buhl, J. A. Orcutt, A. J. Harding, M. E. Kappus, R. S. Detrick, and T. M. Brocher, The structure of 0–0.2-m.y.-old oceanic crust at 9°N on the East Pacific Rise from expanded spread profiles, *J. Geophys. Res.*, *95*, 15,529–15,556, 1990.
- Verosub, K. L., and E. M. Moores, Tectonic rotations in extensional regimes and their paleomagnetic consequences for oceanic basalts, *J. Geophys. Res.*, *86*, 6335–6349, 1981.
- Wessel, P., and W. H. F. Smith, *The Generic Mapping Tools (GMT) version 3.4 Technical Reference & Cookbook*, SOEST/NOAA, 2001.
- White, S. M., K. C. Macdonald, and R. M. Haymon, Basaltic lava domes, lava lakes, and volcanic segmentation on the southern East Pacific Rise, *J. Geophys. Res.*, *105*, 23,519–23,536, 2000.
- Wilcock, W. S. D., D. R. Toomey, G. M. Purdy, and S. C. Solomon, The renavigation of Sea Beam bathymetric data between 9°N and 10°N on the East Pacific Rise, *Mar. Geophys. Res.*, *15*, 1–12, 1993.
- Wright, D. J., R. Haymon, and D. J. Fornari, Crustal fissuring and its relationship to magmatic and hydrothermal processes on the East Pacific Rise crest (9°12' to 54°N), *J. Geophys. Res.*, *100*, 6097–6120, 1995.
- Yoerger, D. R., A. M. Bradley, B. B. Walden, M.-H. Cormier, and W. B. F. Ryan, Fine-scale seafloor survey in rugged deep-ocean terrain with an autonomous robot, in *Proceedings IEEE International Conference in Robotics Automation, San Francisco*, pp. 1787–1792, 2000a.
- Yoerger, D. R., A. M. Bradley, M.-H. Cormier, W. B. F. Ryan, and B. B. Walden, High resolution mapping of a fast spreading mid ocean ridge with the Autonomous Benthic Explorer, in *Proceedings 11th UUST Conference*, 2000b.